Published in final edited form as:
Magn Reson Med. 2010 March ; 63(3): . doi:10.1002/mrm.22216.

Novel Membrane-Permeable Contrast Agent for Brain Tumor Detection by MRI

Mohanraja Kumar[#], **Zdravka Medarova**[#], **Pamela Pantazopoulos**, **Guangping Dai**, and **Anna Moore**[*]
Athinoula A. Martines Center for Biomedical Imaging, Department of Radiology, Massachusetts General Hospital/Harvard Medical School, Charlestown, MA 02129, USA.

[#] These authors contributed equally to this work.

Abstract

One of the key challenges hindering the clinical intervention against brain cancer is defined by the inability to detect brain tumors at an early enough stage to permit effective therapy. Furthermore, the rapid growth and severe lethality of this form of cancer predicate the vital importance of monitoring the development of the pathology and its outcome after therapeutic intervention. With this in mind, we designed a novel membrane-permeant contrast agent, MN-MPAP-Cy5.5, which consists of a superparamagnetic iron oxide core, for MRI conjugated to myristoylated polyarginine peptides, as a membrane translocation module and labeled with the near-infrared dye Cy5.5 for correlative microscopy. This probe showed a remarkable uptake by U-87 human glioma cells in vitro and localized and delineated stereotactically injected tumor in vivo by MRI. Our findings suggest that the agent mediates its effects by translocation of the magnetic nanoparticles label across the leaky tumor vasculature, followed by enhanced accumulation in tumor cells. The noninvasive detection of brain tumors when they are still small represents a formidable challenge from an imaging standpoint. Our study describes an improved strategy to detect brain lesions by utilizing a contrast agent with membrane translocation properties.

Keywords

BBB; brain tumor; peptide; MR imaging; fluorescence imaging; magnetic nanoparticles; contrast agent

Gliomas are deadly, highly invasive, and highly aggressive primary brain tumors (1). The survival period of patients with gliomas after initial diagnosis is generally limited to 12–14 months. Currently available therapeutic methods for glioma treatment include surgery, chemotherapy, radiation therapy, and, as a very recent option, gene therapy (2,3). However, each of these methods has its limitations. As such, surgical resection often leaves residual tumor mass, which tends to form recurrent tumors due to its infiltrative nature. Similarly, radiation therapy is not efficient at killing residual tumor cells and produces severe side effects such as swelling of the brain tissue surrounding the tumor. Though chemotherapy is one of the well-established treatment methods to control tumor growth, gliomas often become resistant to chemotherapeutic drugs (1,4). Even with the introduction of new treatment methods that include direct tumoral injection of chemotherapeutics,

[*]Correspondence to: MGH/MIT/HMS Athinoula A. Martinos Center for Biomedical Imaging, Department of Radiology, Massachusetts General Hospital/Harvard Medical School, Rm. 2301, Bldg. 149, 13th St., Charlestown, MA 02129. amoore@helix.mgh.harvard.edu.

permeabilization of the blood-brain barrier, and combination of drugs and/or surgery and radiation therapy, the success in treating glioma tumors is still far from satisfactory (5,6). Gene therapy using HSV-tk (herpes simplex virus thymidine kinase gene) with ganciclovir has shown considerable success in clinical trials (7), but the high recurrence rate and heterogeneity of gliomas present significant obstacles to its applicability (8).

Clearly, identification of true tumor borders during the diagnosis and treatment phases would aid tremendously in the clinical management of gliomas. Noninvasive imaging, including MRI, CT, and Positron Emission Tomography (PET), has played a central role in the early diagnosis and therapeutic monitoring of brain tumors (9–11). MR contrast agents, for example, gadolinium (Gd) (III) chelates and superparamagnetic iron oxide nanoparticles, play a key role in characterization and localization of tumors (12–14). Despite the wide application of Gd-chelate based contrast agents, recent reports have associated them with undesirable effects such as spurious hypocalcemia, transmetallation, immunogenicity, and contrast-mediated nephropathy resulting from their incomplete elimination (15,16). Furthermore, the low retention time of these agents in the blood pool and the need for a high local concentration in order to induce sufficient contrast make the application of these agents problematic, particularly in severely ill patients. By contrast, iron oxide nanoparticles can be detected with a high sensitivity, are biocompatible (17), and have routinely been used for imaging tumor associated micro-vessels (18–21).

The blood-brain barrier is composed of high-density cells restricting passage of substances from the bloodstream to the brain (22). Owing to the unique nature of the brain endothelium, delivery of therapeutics and contrast agents such as magnetic nanoparticles (MN) across the intact blood-brain barrier presents a formidable challenge. However, this situation is simplified in gliomas, where the endothelial barrier is compromised and shows significant leakiness, leading to accumulation of contrast agents in the tumor interstitium (23,24). For instance, in U-87 glioma tumor model, blood-brain barrier breakdown leads to pores ranging from 7–100 nm in size, a range capable of accommodating certain nanoparticles (25). Hence, the goal of this study was to improve the detection of gliomas by MRI using membrane-permeant superparamagnetic iron oxides associated with a very significant accumulation in brain tumors. This effect is likely mediated by translocation across the leaky tumor vasculature and the tumor cell membrane, followed by contrast agent residence inside the tumor cells. We believe that the novel contrast agent described here can serve as a sensitive tool for detecting brain tumors and, possibly, following their fate after therapy.

MATERIALS AND METHODS

Synthesis of Myristoyl-Substituted β-Alanine

Synthesis was performed as previously reported (26). β-alanine (890 mg, 10.0 mmol) and K_2CO_3 (430 mg per mmol of β-alanine) were dissolved in 40 mL of water and cooled to 0°C. Myristoyl chloride was dissolved in 40 mL of acetone and added dropwise while stirring was continued. The reaction mixture was maintained at 0°C for 1 h and then allowed to stir for additional 1 h at room temperature. Most of the acetone was removed by rotavapor and the remaining aqueous solution was acidified by concentrated HCl to pH = 1. The precipitate was collected, washed with water, dried, and obtained as colorless powder (94%).

Solid-Phase Peptide Synthesis

Peptide was synthesized by Fmoc solid phase chemistry using 2-6H-Benzotriazole-1-yl-9,1,3,3-tetramethylaminium hexa fluorophosphate (HBTU) and 1-hydroxybenzotriazole (HOBt) activating agents. All amino acids and resin were purchased from Nova Biochem,

USA. All other reagents were purchased from Advanced Chemtech, Sigma-Aldrich, GE Healthcare, and Fisher-Scientific and used without further purifications. The sequence β-Ala(Mys)-Arg-Arg-Arg-Arg-Arg-Arg-Arg-Cys-NH_2 was synthesized in 0.1 mmol scale of Rink amide methyl benzyl hydro amine (MBHA) resin, cleaved by 5 mL of cocktail mixture (94% TFA + 2.5% water + 2.5% ethanedithiol + 1% triisopropyl silane), precipitated in cold ether, purified by reverse phase (RP)-high-performance liquid chromatography using eluting solvents A and B (A = 0.1% trifluoroacetic acid (TFA) in water and B = 0.1% TFA in acetonitrile), and characterized by matrix-assisted laser desorption ionization mass spectrometry (MALDI-MS); 1494.91 calculated (cald.) and 1495.33 (found).

MN-MPAP-Cy5.5 Probe Synthesis

The preparation of aminated MN was reported previously (27). To attach the Cy5.5 monofunctional dye to nanoparticles, 1 mL of aminated iron oxide nanoparticles with the pH adjusted to 9.6 in 0.5 M sodium bicarbonate was added to 1 mg of monofunctional Cy5.5 NHS ester (Amersham-Pharmacia; catalog no. Q15408) and incubated on a rotator overnight at room temperature. After incubation, the mixture was purified from nonreacted dye on a G-25 Sephadex column equilibrated with 20 mM sodium citrate buffer with 0.15 M NaCl, pH 8.0. Next, the thioether bond was introduced onto nanoparticles by reaction with the hetero bifunctional group succinimidyl iodoacetate. The reaction mixture was incubated for 15 min and then purified on G-25 Sephadex column equilibrated with 20 mM Na-citrate buffer with 0.15 M NaCl, pH 6.5. In the next step, myristoylated polyarginine peptide (MPAP) peptide was added to nanoparticles at the ratio of 1:10 and incubated for 2 h. Finally, the MN-MPAP-Cy5.5 probe was purified using a Sephadex G-25 column equilibrated with 20 mM Nacitrate buffer with 0.15 M NaCl, pH 8.0.

The probe was characterized spectrophotometrically for iron content, number of Cy5.5 dye molecules per nanoparticle, and number of peptides per nanoparticle.

MN labeled with Cy5.5 without MPAP (MN-Cy5.5) were synthesized as well and served as control in our studies. Nanoparticle size measurements were performed using Zetasizer Nano Zs (Malvern Instruments Ltd., Worcestershire, UK).

Quantitative Cell Uptake Studies

To compare the cellular uptake of MN-MPAP-Cy5.5 and MN-Cy5.5, we performed cell uptake studies with a fixed number of U-87 human glioblastoma cells. Cells (30,000/well) were incubated with increasing iron concentrations (0–60 μg/mL of Fe) for 24 h at 37°C in a humidified CO_2 atmosphere. Then the cells were washed with 1× phosphate-buffered saline buffer and lysed using a freeze-thaw method in distilled water. The solution was centrifuged and supernatants were used for fluorescence measurements at 674 nm (excitation) and 710 nm (emission), with a cutoff of 695 nm. The results were expressed as relative cell fluorescence normalized to total cell protein.

Confocal Microscopy

Intracellular distribution of MN-MPAP-Cy5.5 and MN-Cy5.5 probes within U-87 cell lines was visualized by fluorescence microscopy. Cells were grown on coverslips overnight, incubated with MN-MPAP-Cy5.5 or MN-Cy5.5 (50 μg/mL of Fe) for 24 h, washed and fixed with 4% paraformaldehyde. Confocal microscopy was performed using an Axiovert 200M inverted microscope (Carl Zeiss, Inc., Thornwood, NY) equipped with an LSM Pascal Vario RGB Laser Module (Arg 458/488/514 nm, HeNe 543 nm, HeNe 633 nm). Images with a slice thickness of <0.9 μm were acquired to produce Cy5.5 staining, as well as Nomarski optics.

Fluorescence-Activated Cell Sorting Analysis (FACS)

To evaluate the relative uptake of MN-MPAP-Cy5.5 and MN-Cy5.5 in the U-87 cell line, FACS analysis was performed. Cells were incubated with MN-MPAP-Cy5.5 or MN-Cy5.5, washed, and subjected to FACS analysis in FL4 channel using an automated FACS machine (BD FACS Calibur; Becton Dickinson Biosciences, San Jose, CA).

Iron Quantification in U-87 Cells

To quantitate iron uptake in U-87 cells, MN-MPAP-Cy5.5 and MN-Cy5.5 probes were incubated with 50 μg/mL of iron for 24 h, washed, trypsinized, and counted. The cells were then dissolved in 6-N HCl and heated to 90°C. The amount of iron in cell lysates was determined using Total Iron Reagent Set (Pointe Scientific, Canton, MI). Each experiment was performed in triplicate. The results were read at 540 nm and expressed as picograms of iron per microgram of total cell protein.

In Vivo MR Imaging

U-87 human glioma cells (~3 million) were injected stereotactically in the brain of nude mice ($n = 7$) and allowed to grow for approximately 2 to 3 weeks. Tumor-bearing mice were then injected intravenously with MN-MPAP-Cy5.5 or MN-Cy5.5 probes (10 mg Fe/kg). Nontumor-bearing mice served as controls. Before and 24 h after injection, mice were imaged using 9.4T Bruker (Billerica, MA) horizontal bore scanner equipped with Para Vision 3.0 software. The imaging protocol consisted of coronal and transverse T_2-weighted spin echo pulse sequences. To obtain T_2 maps, the following parameters were used: spin echo pulse repetition time/echo time = 3000/8, 16, 24, 32, 40, 48, 56, 64; field of view = 19.2 × 19.2 mm; matrix size 128 × 128; slice thickness = 0.5 mm; resolution 0.15 × 0.15 mm; imaging times of 4.0 min and 16 sec. Image reconstruction was performed using Marevisi 3.5 software (Institute for Biodiagnostics, National Research Council, Canada). T_2 relaxation times were determined by T_2 map analyses of regions of interest drawn around the tumors.

Image Analysis

Regions of interest were drawn around the tumors. T_2 relaxation times were determined from T_2 maps. The terminal slices were not included in the analyses to avoid interference from partial-volume effects. Relative accumulations of MN-MPAP-Cy5.5 and MN-Cy5.5 were estimated based on the following method: T_2 before injection – T_2 after injection of MN-MPAP-Cy5.5 against T_2 before injection – T_2 after injection of MN-Cy5.5 by using a Student t test.

Histology

After the final MR session, the brains were snap frozen and sliced into 7-μm slices. Consecutive sections were stained for hematoxylin and eosin and 3,3′-diaminobenzidine-enhanced Prussian Blue stain (for iron). Separate sections were processed for fluorescence microscopy in Cy5.5 channel and macrophage staining. For macrophage staining, the tissue sections were blocked with 5% serum and then exposed sequentially to macrophage-specific primary antibody (CD-68 rat-antimouse; Serotec) and secondary antibody (goat-antirat-rhodamine; Abcam). Histologic slides were covered with coverslips, mounted with VectaShield 4′,6-diamidino-2-phenylindole (DAPI)-containing medium (Vector Laboratories), and visualized using a fluorescence microscope.

All animal experiments were performed in compliance with institutional guidelines and according to the animal protocol approved by the Subcommittee on Research Animals Care at Massachusetts General Hospital.

RESULTS

Probe Synthesis, Characterization, and In Vitro Studies

To synthesize membrane-permeant nanoparticles capable of accumulating in brain tumors, we conjugated MPAP (26) to iron oxide nanoparticles modified with fluorescent Cy5.5 dye. The MN-MPAP-Cy5.5 nanoparticles were characterized and shown to consist of four Cy5.5 dye molecules and eight peptide molecules per iron oxide nanoparticle and were 40 nm in size. Schematic representation of the synthesis is shown in Fig. 1. Characterization of the peptide by high-performance liquid chromatography and mass analysis are presented in Supplemental Figs. 1 and 2.

To compare the cellular uptake of MN-MPAP-Cy5.5 and MN-Cy5.5, we performed studies in U-87 human glioblastoma cells. First we performed a fluorescence-based uptake study on cell lysates, following incubation with increasing concentrations of MN-MPAP-Cy5.5 or MN-Cy5.5. The uptake of MN-MPAP-Cy5.5 reached a plateau at around 40 μg/mL of Fe. There was a significantly higher uptake of MN-MPAP-Cy5.5 compared to MN-Cy5.5 at all concentrations tested (Fig. 2a). Direct measurement of the amount of iron associated with the cells also showed a significantly higher accumulation of MN-MPAP-Cy5.5 compared to MN-Cy5.5 ($P < 0.0001$; Fig. 2b). To further confirm our observations, we performed flow cytometric experiments with the U-87 cell line. We incubated cells with MN-MPAP-Cy5.5 and MN-Cy5.5 and evaluated fluorescence in the FL4 channel (derived from the Cy5.5 label). As we expected, there was a significant shift in fluorescence in the cells stained with MN-MPAP-Cy5.5 compared to the cells incubated with the control MN-Cy5.5 probe (Fig. 2c). Quantitative analysis revealed a 30-fold difference in fluorescence between the two probes (Fig. 2d). To evaluate the intracellular distribution of the probe, we performed confocal microscopy with MN-MPAP-Cy5.5 and MN-Cy5.5. Figure 3 demonstrated that the MN-MPAP-Cy5.5 probe was distributed to the cytoplasm. In addition, the overall accumulation of MN-MPAP-Cy5.5 in the cells was significantly higher than that of MN-Cy5.5, taking into account that the same concentrations of the probes were added to the cells. These data corroborated our quantitative cell labeling studies described above.

In Vivo Studies

To assess the feasibility of utilizing MN-MPAP-Cy5.5 for in vivo imaging of brain tumors in a mouse model of glioma, we stereotactically injected nude mice with human U-87 cells. T_2-weighted MRI was performed on tumor-bearing animals before and 24 h after probe injection. Representative T_2 images are shown in Fig. 4a. There was a distinctive area of signal loss associated with the tumors following injection of MN-MPAP-Cy5.5. By contrast, there was no visible difference in tumor-associated signal intensity before and after injection of MN-Cy5.5. Analysis of T_2 maps of the same animals (Fig. 4b) revealed a significant shortening of the tumor-associated T_2 relaxation time following injection of MN-MPAP-Cy5.5 but not MN-Cy5.5 ($P = 0.05$). Nontumor-bearing animals showed no change in T_2 after injection of MN-MPAP-Cy5.5 (Supplemental Fig. 3).

After the final MRI session, the brains were subjected to correlative histology. Consecutive sections were stained to evaluate differences in uptake between the MN-MPAP-Cy5.5 and MN-Cy5.5 probes. There was a detectable 3,3′-diaminobenzidine-enhanced Prussian Blue staining in the sections derived from MN-MPAP-Cy5.5-injected animals, whereas the sections from MN-Cy5.5-injected mice showed considerably less iron staining (Fig. 5a). To further confirm the differential probe accumulation, sections were examined by fluorescence microscopy to detect Cy5.5 staining. Sections from MN-MPAP-Cy5.5-injected animals showed abundant Cy5.5 signal compared to animals injected with the MN-Cy5.5 probe (Fig. 5b).

Gliomas are typically infiltrated with tumor-recruited macrophages, which take up the probe and thus contribute to the signal on MR images. To determine the input of macrophage uptake, we performed dual-channel fluorescence microscopy of tumor sections (Fig. 6). Most of the macrophage population was located at the tumor periphery, with a subset of cells showing positive Cy5.5 staining. Visually, there was no noticeable difference in macrophage probe accumulation between MN-MPAP-Cy5.5 and MN-Cy5.5, whereas total uptake by the tumor cells in the tumor core and periphery was considerably higher for MN-MPAP-Cy5.5. This result showed that the input from macrophage uptake of the probe on MR signal would be similar for both probes, and the observed difference in T_2 between MN-MPAP-Cy5.5 and MN-Cy5.5 was due to the higher accumulation of MN-MPAP-Cy5.5 in tumor cells.

DISCUSSION AND CONCLUSION

According to statistics from the year 2000, 45,000 people suffer from brain tumors, accounting for 15,000 deaths annually in the United States (28). Consequently, there is an urgent need in oncology and neurology to develop methods for early detection and monitoring of neoplasia in the brain. In this study, we utilized modified polyarginine peptides attached to iron oxide nanoparticles for imaging of brain tumors after intravenous injection. It has been reported previously by our group that the myristoylated polyarginine peptide could cross the blood-brain barrier, followed by localization to the cytoplasm (26). We speculated that by conjugating MPAP peptide to an imaging agent, we would facilitate penetration through the leaky tumor vasculature, followed by uptake by tumor cells. The rationale for this was based on the fact that acylated peptides/proteins increase membrane permeability and improve proteolytic stability and specificity of cellular localization (29,30). Furthermore, the permeability of the peptide is due to the guanidino group of the arginine, which has a pK ~12 and therefore facilitates intracellular delivery of other molecules, providing that they are conjugated to the peptide. In addition, it has been previously shown that the uptake of fatty acylated polyarginine peptide in HeLa cells was 7-fold higher compared to nonacylated polyarginine peptide in HeLa cells (31). It has also been shown that peptides containing myristic acid (14-carbon) provide sufficient energy to anchor to a biologic membrane compared to, for example, a palmitic acid (16-carbon) chain and therefore possess efficient cell-crossing capability without toxicity (32).

The efficient cell-penetrating capability of our imaging probe was first tested in vitro in U-87 glioma cells and then in vivo in a mouse model of human glioma. Our quantitative cell uptake studies demonstrated preferential accumulation of MN-MPAP-Cy5.5 in cells compared to unconjugated parental nanoparticles. These studies were corroborated by fluorescence microscopy and FACS analysis. Specifically, fluorescence microscopy revealed significant cytoplasmic accumulation of the contrast agent delivered by MPAP. The in vivo MRI studies showed a significant difference in probe accumulation in U-87 tumors, judged by a significantly greater drop in T_2 in MN-MPAP-Cy5.5-injected animals.

Since tumor-infiltrating macrophages are capable of accumulating an imaging probe and therefore producing signal on MR images, it was important to estimate the contribution of this signal to the overall T_2 of the tumor. Dual-channel fluorescence microscopy revealed that there was nearly equivalent accumulation of both probes in tumor-associated macrophages. This seemingly counterintuitive result could be explained by the high phagocytic rate in macrophages (33,34) where the presence of MPAP would not contribute to the overall uptake in these cells. Tumor cells in turn have a low phagocytic rate, and therefore the impact of MPAP on cellular accumulation of the probe is far more pronounced in these cells. This hypothesis was confirmed by ex vivo histology of tumor sections, where

tumor cells showed significantly more intense iron staining in the case of MN-MPAP compared to parental nanoparticles.

Due to the poor prognosis of glioma tumors, treatment benefits remain limited (35), despite the recent gains in knowledge about the disease (36). Still, the assessment of therapeutic success remains a challenge because of the high propensity of this type of tumor to infiltrate normal healthy brain tissue, making surgery, radiation, and chemotherapy ineffective in the long run. MRI is routinely used in the clinic to detect gliomas. However, studies investigating the capacity of MRI to delineate the tumor boundaries of gliomas are scarce. Some studies used image-guided tumor biopsy or postmortem specimens for correlation and reported on discrepancies between the real tumor extent and findings by MRI (37–40).

In the context of these challenges, the value of our method is understandable. Through the enhanced delivery of iron nanoparticles to the tumor cells, we effectively improved the contrast between the tumor and surrounding tissue, making tumor identification and delineation less ambiguous. However, at this point we do not know the smallest tumor size that these nanoparticles could detect. We believe that with this tool in hand, more accurate measurement of the dynamics of tumor growth, especially in response to therapy, would be possible. Furthermore, unlike gadolinium, iron nanoparticles help to identify tumor area signal changes that persist for 2–5 days postadministration (19,41,42). Our nanoparticles have the additional advantage of providing a method to directly monitor the glioma cells and could thus be applied to postoperative imaging following tumor resection. Another potential clinical application includes visualizing blood-brain barrier disruptions that are not detectable by gadolinium-enhanced MR in human infarcts (43).

An additional value of our nanoparticles may directly extend from the membrane-translocating properties of the agent. Therapy directed toward angiogenesis normalization can compromise tumor imaging by MRI, since it can limit the access of conventional contrast agents to the tumor. The leakiness of the tumor endothelium is key for tumor detection using unmodified iron oxides or Gd chelates. In earlier studies, we have shown that in fact MPAP can deliver a near-infrared dye across the blood-brain barrier (44). Consequently, it is not inconceivable that even in the cases of vascular normalization, the overall uptake of MPAP-based contrast agents by tumor cells will be sufficient for tumor visualization. Studies of that nature are under way at our laboratory.

Finally, because of the overall higher tumor/tumor cell loading with contrast agent in the presence of MPAP and the higher contrast revealed by our studies, it is likely that our method will increase the reliability of detection of tumors that are difficult to distinguish from background using standard methods. This will be particularly important in scenarios such as therapeutic monitoring, early diagnosis, and detection of recurrence. With high tumor cell loading with contrast agent, as seen in cell tracking studies, it is possible to detect even a single cell in the brain (45), extending the potential application of our model for the detection of tumor recurrence or metastatic spread of various forms of cancer that disseminate to the brain.

In summary, this study demonstrated the advantage of a new, MPAP-modified MR contrast agent for brain tumor detection. In the future, we plan to apply this agent for monitoring tumor response to therapy using clinically relevant animal models and imaging equipment.

Supplementary Material

Refer to Web version on PubMed Central for supplementary material.

Acknowledgments

The authors thank Dr. Rona Carroll (Brigham and Women's Hospital, Boston) for invaluable help with the animal model used in this study. This study was supported in part by the K99/R00 CA129070 to Z.M.

REFERENCES

1. Burton EC, Prados MD. Malignant gliomas. Curr Treat Options Oncol. 2000; 1:459–468. [PubMed: 12057153]
2. Candolfi M, Curtin JF, Nichols WS, Muhammad AG, King GD, Pluhar GE, McNiel EA, Ohlfest JR, Freese AB, Moore PF, Lerner J, Lowenstein PR, Castro MG. Intracranial glioblastoma models in preclinical neuro-oncology: neuropathological characterization and tumor progression. J Neurooncol. 2007; 85:133–148. [PubMed: 17874037]
3. Prados MD, McDermott M, Chang SM, Wilson CB, Fick J, Culver KW, Van Gilder J, Keles GE, Spence A, Berger M. Treatment of progressive or recurrent glioblastoma multiforme in adults with herpes simplex virus thymidine kinase gene vector-producer cells followed by intravenous ganciclovir administration: a phase I/II multi-institutional trial. J Neurooncol. 2003; 65:269–278. [PubMed: 14682377]
4. Kleinberg L, Grossman SA, Carson K, Lesser G, O'Neill A, Pearlman J, Phillips P, Herman T, Gerber M. Survival of patients with newly diagnosed glioblastoma multiforme treated with RSR13 and radiotherapy: results of a phase II new approaches to brain tumor therapy CNS consortium safety and efficacy study. J Clin Oncol. 2002; 20:3149–3155. [PubMed: 12118029]
5. Warren KE, Patel MC, Aikin AA, Widemann B, Libucha M, Adamson PC, Neuwirth R, Benziger D, O'Toole T, Ford K, Patronas N, Packer RJ, Balis FM. Phase I trial of lobradimil (RMP-7) and carboplatin in children with brain tumors. Cancer Chemother Pharmacol. 2001; 48:275–282. [PubMed: 11710627]
6. Adam JF, Biston MC, Joubert A, Charvet AM, Le Bas JF, Esteve F, Elleaume H. Enhanced delivery of iodine for synchrotron stereotactic radiotherapy by means of intracarotid injection and blood-brain barrier disruption: quantitative iodine biodistribution studies and associated dosimetry. Int J Radiat Oncol Biol Phys. 2005; 61:1173–1182. [PubMed: 15752899]
7. Pulkkanen KJ, Yla-Herttuala S. Gene therapy for malignant glioma: current clinical status. Mol Ther. 2005; 12:585–598. [PubMed: 16095972]
8. Fulci G, Chiocca EA. The status of gene therapy for brain tumors. Expert Opin Biol Ther. 2007; 7:197–208. [PubMed: 17250458]
9. Price P. PET as a potential tool for imaging molecular mechanisms of oncology in man. Trends Mol Med. 2001; 7:442–446. [PubMed: 11597518]
10. Gerstner ER, Sorensen AG, Jain RK, Batchelor TT. Advances in neuroimaging techniques for the evaluation of tumor growth, vascular permeability, and angiogenesis in gliomas. Curr Opin Neurol. 2008; 21:728–735. [PubMed: 18989120]
11. Ellika SK, Jain R, Patel SC, Scarpace L, Schultz LR, Rock JP, Mikkelsen T. Role of perfusion CT in glioma grading and comparison with conventional MR imaging features. AJNR Am J Neuroradiol. 2007; 28:1981–1987. [PubMed: 17893216]
12. Gambarota G, Leenders W, Maass C, Wesseling P, van der Kogel B, van Tellingen O, Heerschap A. Characterisation of tumour vasculature in mouse brain by USPIO contrast-enhanced MRI. Br J Cancer. 2008; 98:1784–1789. [PubMed: 18506183]
13. Bulte JW. Intracellular endosomal magnetic labeling of cells. Methods Mol Med. 2006; 124:419–439. [PubMed: 16506433]
14. Moore A, Marecos E, Bogdanov A Jr, Weissleder R. Tumoral distribution of long-circulating dextran-coated iron oxide nanoparticles in a rodent model. Radiology. 2000; 214:568–574. [PubMed: 10671613]
15. Tien RD, Brasch RC, Jackson DE, Dillon WP. Cerebral Erdheim-Chester disease: persistent enhancement with Gd-DTPA on MR images. Radiology. 1989; 172:791–792. [PubMed: 2772189]
16. Baxter AB, Melnikoff S, Stites DP, Brasch RC. AUR Memorial Award 1991. Immunogenicity of gadolinium-based contrast agents for magnetic resonance imaging: induction and characterization of antibodies in animals. Invest Radiol. 1991; 26:1035–1040. [PubMed: 1722486]

17. Bourrinet P, Bengele HH, Bonnemain B, Dencausse A, Idee JM, Jacobs PM, Lewis JM. Preclinical safety and pharmacokinetic profile of ferumoxtran-10, an ultrasmall superparamagnetic iron oxide magnetic resonance contrast agent. Invest Radiol. 2006; 41:313–324. [PubMed: 16481915]
18. Tropres I, Lamalle L, Peoc'h M, Farion R, Usson Y, Decorps M, Remy C. In vivo assessment of tumoral angiogenesis. Magn Reson Med. 2004; 51:533–541. [PubMed: 15004795]
19. Varallyay P, Nesbit G, Muldoon LL, Nixon RR, Delashaw J, Cohen JI, Petrillo A, Rink D, Neuwelt EA. Comparison of two superparamagnetic viral-sized iron oxide particles ferumoxides and ferumoxtran-10 with a gadolinium chelate in imaging intracranial tumors. AJNR Am J Neuroradiol. 2002; 23:510–519. [PubMed: 11950637]
20. Brillet PY, Gazeau F, Luciani A, Bessoud B, Cuenod CA, Siauve N, Pons JN, Poupon J, Clement O. Evaluation of tumoral enhancement by superparamagnetic iron oxide particles: comparative studies with ferumoxtran and anionic iron oxide nanoparticles. Eur Radiol. 2005; 15:1369–1377. [PubMed: 15726379]
21. Taschner CA, Wetzel SG, Tolnay M, Froehlich J, Merlo A, Radue EW. Characteristics of ultrasmall superparamagnetic iron oxides in patients with brain tumors. AJR Am J Roentgenol. 2005; 185:1477–1486. [PubMed: 16304001]
22. Abbott NJ, Ronnback L, Hansson E. Astrocyte-endothelial interactions at the blood-brain barrier. Nat Rev Neurosci. 2006; 7:41–53. [PubMed: 16371949]
23. Jain RK. Transport of molecules across tumor vasculature. Cancer Metastasis Rev. 1987; 6:559–593. [PubMed: 3327633]
24. Dvorak HF, Nagy JA, Feng D, Brown LF, Dvorak AM. Vascular permeability factor/vascular endothelial growth factor and the significance of microvascular hyperpermeability in angiogenesis. Curr Top Microbiol Immunol. 1999; 237:97–132. [PubMed: 9893348]
25. Hobbs SK, Monsky WL, Yuan F, Roberts WG, Griffith L, Torchilin VP, Jain RK. Regulation of transport pathways in tumor vessels: role of tumor type and microenvironment. Proc Natl Acad Sci U|S|A. 1998; 95:4607–4612. [PubMed: 9539785]
26. Pham W, Zhao BQ, Lo EH, Medarova Z, Rosen B, Moore A. Crossing the blood-brain barrier: a potential application of myristoylated polyarginine for in vivo neuroimaging. Neuroimage. 2005; 28:287–292. [PubMed: 16040255]
27. Josephson L, Tung CH, Moore A, Weissleder R. High-efficiency intra-cellular magnetic labeling with novel superparamagnetic-Tat peptide conjugates. Bioconjug Chem. 1999; 10:186–191. [PubMed: 10077466]
28. Greenlee RT, Murray T, Bolden S, Wingo PA. Cancer statistics. CA Cancer J Clin. 2000; 50:7–33. [PubMed: 10735013]
29. Dunphy JT, Linder ME. Signalling functions of protein palmitoylation. Biochim Biophys Acta. 1998; 1436:245–261. [PubMed: 9838145]
30. Resh MD. Fatty acylation of proteins: new insights into membrane targeting of myristoylated and palmitoylated proteins. Biochim Biophys Acta. 1999; 1451:1–16. [PubMed: 10446384]
31. Pham W, Kircher MF, Weissleder R, Tung CH. Enhancing membrane permeability by fatty acylation of oligoarginine peptides. Chembiochem. 2004; 5:1148–1151. [PubMed: 15300843]
32. Galbiati F, Guzzi F, Magee AI, Milligan G, Parenti M. Chemical inhibition of myristoylation of the G-protein Gi1 alpha by 2-hydroxymyristate does not interfere with its palmitoylation or membrane association. Evidence that palmitoylation, but not myristoylation, regulates membrane attachment. Biochem J. 1996; 313:717–720. [PubMed: 8611146]
33. Fadok VA, Bratton DL, Konowal A, Freed PW, Westcott JY, Henson PM. Macrophages that have ingested apoptotic cells in vitro inhibit proinflammatory cytokine production through autocrine/paracrine mechanisms involving TGF-beta, PGE2, and PAF. J Clin Invest. 1998; 101:890–898. [PubMed: 9466984]
34. Yuan A, Chen JJ, Yang PC. Pathophysiology of tumor-associated macrophages. Adv Clin Chem. 2008; 45:199–223. [PubMed: 18429498]
35. Norden AD, Wen PY. Glioma therapy in adults. Neurologist. 2006; 12:279–292. [PubMed: 17122724]
36. Phillips HS, Kharbanda S, Chen R, Forrest WF, Soriano RH, Wu TD, Misra A, Nigro JM, Colman H, Soroceanu L, Williams PM, Modrusan Z, Feuerstein BG, Aldape K. Molecular subclasses of

high-grade glioma predict prognosis, delineate a pattern of disease progression, and resemble stages in neurogenesis. Cancer Cell. 2006; 9:157–173. [PubMed: 16530701]

37. Watanabe M, Tanaka R, Takeda N. Magnetic resonance imaging and histopathology of cerebral gliomas. Neuroradiology. 1992; 34:463–469. [PubMed: 1436452]
38. Jansen EP, Dewit LG, van Herk M, Bartelink H. Target volumes in radiotherapy for high-grade malignant glioma of the brain. Radiother Oncol. 2000; 56:151–156. [PubMed: 10927133]
39. Nishi N, Kawai S, Yonezawa T, Fujimoto K, Masui K. Early appearance of high grade glioma on magnetic resonance imaging. Neurol Med Chir. 2009; 49:8–12.
40. Scarabino T, Popolizio T, Trojsi F, Giannatempo G, Pollice S, Maggialetti N, Carriero A, Di Costanzo A, Tedeschi G, Salvolini U. Role of advanced MR imaging modalities in diagnosing cerebral gliomas. Radiol Med. 2008; 114:448–460. [PubMed: 19082784]
41. Neuwelt EA, Varallyay P, Bago AG, Muldoon LL, Nesbit G, Nixon R. Imaging of iron oxide nanoparticles by MR and light microscopy in patients with malignant brain tumours. Neuropathol Appl Neurobiol. 2004; 30:456–471. [PubMed: 15488022]
42. Trehin R, Figueiredo JL, Pittet MJ, Weissleder R, Josephson L, Mah-mood U. Fluorescent nanoparticle uptake for brain tumor visualization. Neoplasia. 2006; 8:302–311. [PubMed: 16756722]
43. Saleh A, Schroeter M, Jonkmanns C, Hartung HP, Modder U, Jander S. In vivo MRI of brain inflammation in human ischaemic stroke. Brain. 2004; 127:1670–1677. [PubMed: 15128622]
44. Leenders WP, Kusters B, Verrijp K, Maass C, Wesseling P, Heerschap A, Ruiter D, Ryan A, de Waal R. Antiangiogenic therapy of cerebral melanoma metastases results in sustained tumor progression via vessel co-option. Clin Cancer Res. 2004; 10:6222–6230. [PubMed: 15448011]
45. Heyn C, Bowen CV, Rutt BK, Foster PJ. Detection threshold of single SPIO-labeled cells with FIESTA. Magn Reson Med. 2005; 53:312–320. [PubMed: 15678551]

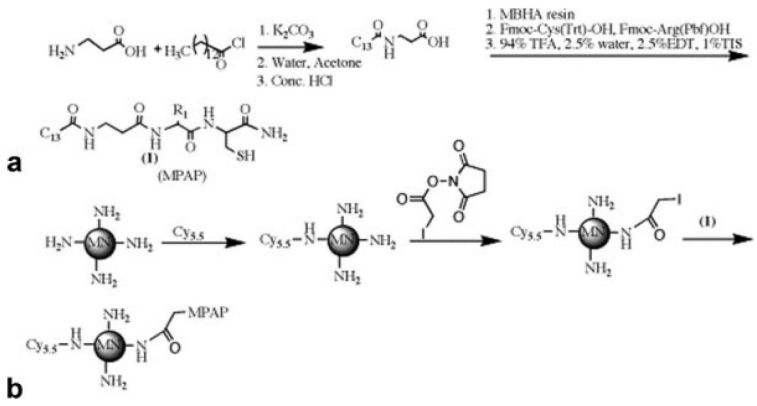

FIG. 1.

Synthesis of MN-MPAPCy5.5 probe. **a:** Synthesis of myristoyl-substituted β-alanine. **b:** Attachment of the peptide to the nanoparticle.

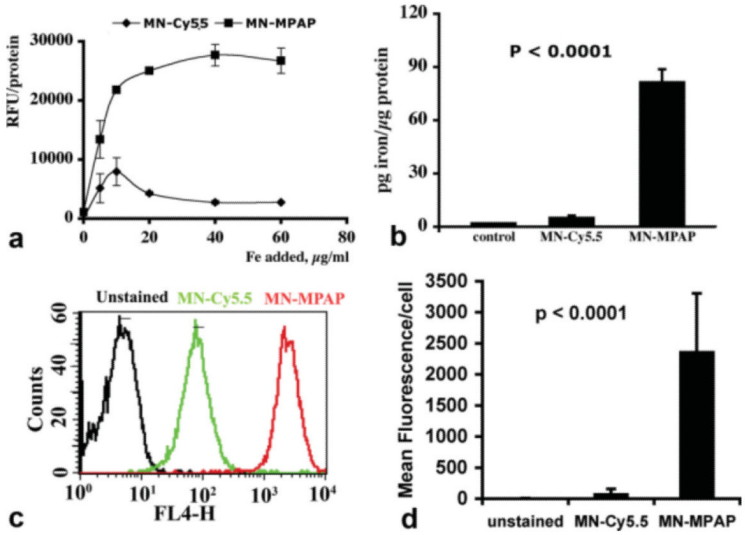

FIG. 2.

Cellular uptake of the probe. **a:** Cells were incubated with MN-MPAP-Cy5.5 and MN-Cy5.5 probes at increasing iron concentrations (0–60 μg/mL of Fe) for 24 h. Fluorescence readout showed significant concentration-dependent increase in MN-MPAP-Cy5.5 accumulation compared to MN-Cy5.5. **b:** Quantitation of cellular iron uptake cells confirmed preferential accumulation of MN-MPAP-Cy5.5 by U-87 cells. **c:** FACS analysis showed significant shift in FL4 channel, signifying superior uptake of MN-MPAP-Cy5.5 by U-87 cells quantitated in (**d**).

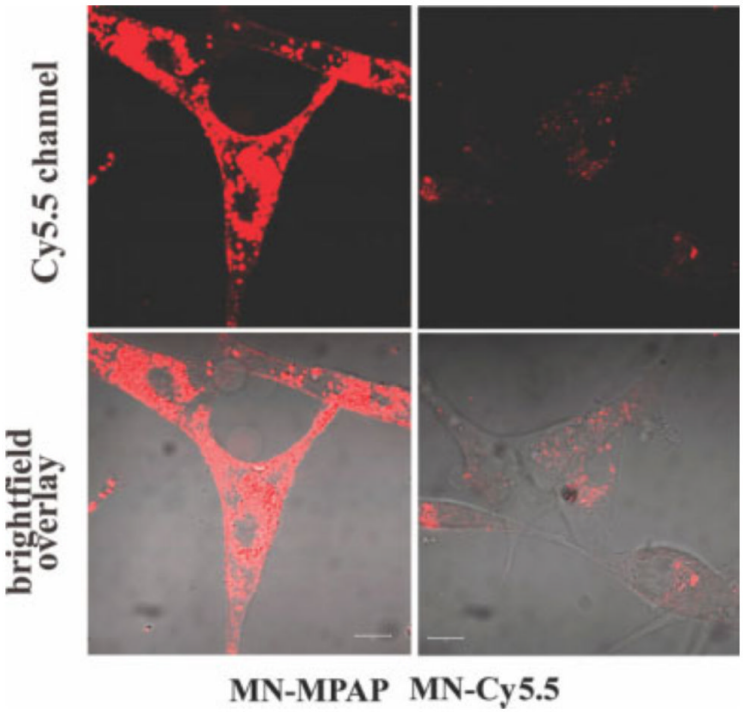

FIG. 3.

Confocal fluorescence microscopy revealed cytoplasmic distribution of MN-MPAP-Cy5.5 probe in U-87 cells. Note that the overall accumulation of MN-MPAP-Cy5.5 MN-MPAP-Cy5.5 in the cells was significantly higher than that of MN-Cy5.5. Magnification bars = 10 μm.

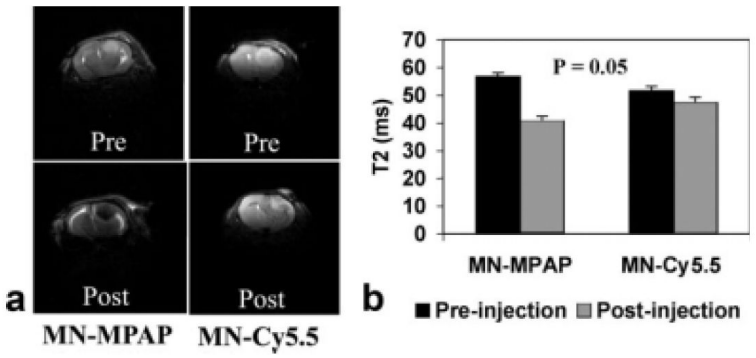

FIG. 4.

In vivo MRI of tumor-bearing animals. **a:** Representative precontrast (top) and postcontrast (bottom) T_2-weighted images of mice injected with MN-MPAP-Cy5.5 and MN-Cy5.5. **b:** Analysis of T_2 maps revealed a marked decrease in T_2 upon accumulation of MN-MPAP-Cy5.5 compared to MN-Cy5.5 ($P = 0.05$).

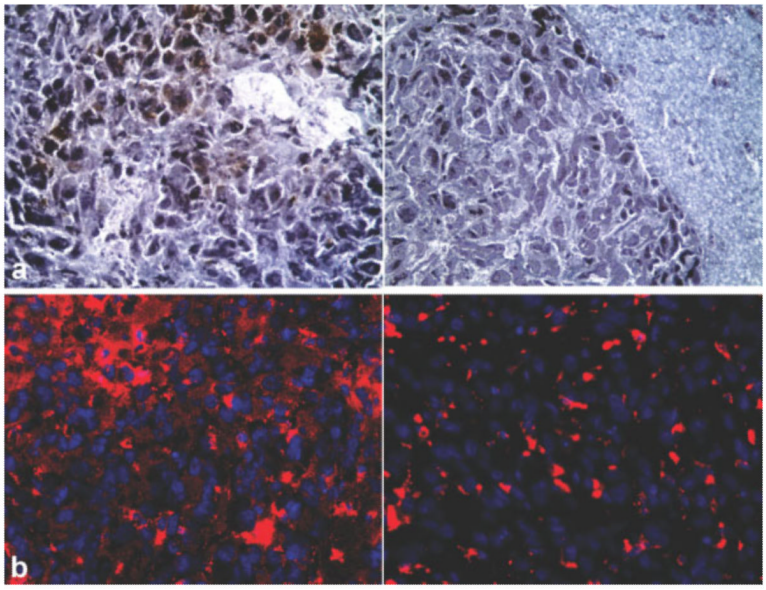

FIG. 5.

Ex vivo microscopy of frozen tumor sections. **a:** 3,3′-Diaminobenzidine enhanced Prussian stain showed a high level of staining in animals with MN-MPAP-Cy5.5-injected tumors compared to the ones injected with MN-Cy5.5. **b:** Corresponding fluorescence microscopy of U-87 stereotactic tumors following injection of MN-MPAP-Cy5.5 or MN-Cy5.5. Preferential accumulation of MN-MPAP-Cy5.5 was confirmed by fluorescence in Cy5.5 channel (depicted in red). Blue: DAPI nuclear stain.

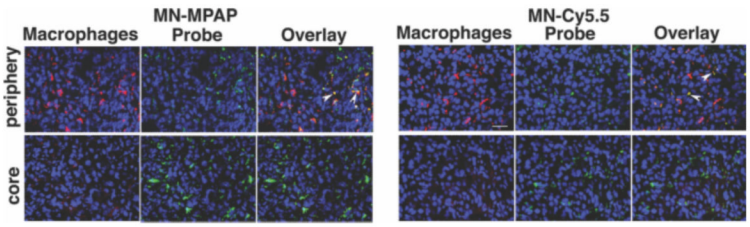

FIG. 6.

Ex vivo microscopy of tumor tissue from MN-MPAP-Cy5.5- and MN-Cy5.5-injected animals. Macrophage staining (red) colocalized with Cy5.5 signal (depicted in green) to a similar degree in both tumors (arrowheads). Tumor cells, in turn, accumulate significantly more MN-MPAP-Cy5.5 than MN-Cy5.5 both in the tumor core and periphery. Magnification bar = 10 μm.